RSC Advances

PAPER

Cite this: *RSC Adv.*, 2020, **10**, 11060

Bioactive silver phosphate/polyindole nanocomposites†

Soumik Podder,[ab] Samrat Paul,[c] Piyali Basak,[c] Bowen Xie,[d] Nigel J. Fullwood,[e] Sara J. Baldock,[f] Ying Yang,[d] John G. Hardy *[fg] and Chandan K. Ghosh *[a]

Received 5th February 2020
Accepted 10th March 2020

DOI: 10.1039/d0ra01129k

rsc.li/rsc-advances

Materials capable of releasing reactive oxygen species (ROS) can display antibacterial and anticancer activity, and may also have anti-oxidant capacity if they suppress intracellular ROS (*e.g.* nitric oxide, NO) resulting in anti-inflammatory activity. Herein we report silver phosphate (Ag_3PO_4)/polyindole (PIn) nanocomposites which display antibacterial, anticancer and anti-inflammatory activity, and have therefore potential for a variety of biomedical applications.

Introduction

Microbial infections are a globally important issue due to the evolution of drug resistant microbes (particularly *Enterococcus faecium*, *S. aureus*, *Klebsiella pneumoniae*, *Acinetobacter baumannii*, *Pseudomonas aeruginosa* and *Enterobacter* species) which are responsible for hospital infections and represent a significant burden for healthcare systems.[1–3] Nanomaterials have gained increasing attention as potential alternatives to antibiotics[3] due to the ease with which we can tailor their properties (*e.g.* particle size, morphology and crystal defects).[4–6] Understanding the mechanism of the antibacterial activity of these nanomaterials is important to control their dosing *in vivo* and any potential environmental impact.[7] The ability of nanomaterials to generate reactive oxygen species (ROS) including superoxide anions ($O_2^{\bullet-}$),[8] hydroxyl radicals ($\cdot OH$),[8] singlet oxygen ($^1O_2$)[9,10] and secondary oxygen centered species such as hydrogen peroxide (H_2O_2) which is developed during the disproportionation of $O_2^{\bullet-}$ which further transforms into $\cdot OH$ and $^1O_2$,[9,10] is of particular interest in regards to toxicity due to the ability of such oxygen centered reactive species to oxidize various cellular constituents.[9,11,12] H_2O_2 can exert oxidative stress on biological systems[9] by generating ROS intracellularly.[13] Intracellular ROS can be endogenous (generated naturally by metabolic processes) or exogenous (generated by other species, *e.g.* nanomaterials).[14] Various nanomaterials display antibacterial activity: *e.g.* ZnO,[15,16] TiO_2,[17,18] MgO,[6] ZnO/TiO_2 nanohybrids,[19] ZnO/$ZnFe_2O_4$,[20] CuO,[21] Ag_3PO_4 (ref. 22) *etc. In vitro* studies detecting ROS derivation from nanomaterials enables the establishment of the underlying mechanism of antibacterial activity to some extent, as the production of different ROS ($O_2^{\bullet-}$, $\cdot OH$ and $^1O_2$) are dependent on the size,[23–25] shape,[24,26,27] and heterostructures of the nanomaterials,[6] but there remains some ambiguity in their mechanism of function.

In addition to ROS-mediated antibacterial activity, non ROS-mediated antibacterial activity caused by the dissolution of cations,[1,23,24,26] internalization of nanostructures,[24] cell membrane disruption,[28] retardation of enzyme activity[3,7] and DNA synthesis,[29] interruption of energy transduction,[3,7] *etc.* are all able to contribute to antibacterial activity. Studies in the scientific literature demonstrate ROS mediated antibacterial activity of different metal oxides for typical durations of 24 h (ref. 6 and 16) to 48 h.[30] Studies of "prolonged exposure" reported either antibacterial activity after long term storage of the nanomaterials repeated exposures[31,32] and the exposure of bacteria to such nanomaterials for durations longer than 24 h with subsequent monitoring of bacterial growth are relatively uncommon.[31,33]

Our understanding of the underlying mechanism of the existing long term antibacterial activity of nanoparticles *in vitro*/*vivo* is still relatively nascent.[34] The simultaneous existence of ROS and non ROS mediated long term antibacterial activity in nanomaterials is therefore an important area of research. Nanomaterials that produce ROS′ can be used to treat cancer cells,[35,36] with cell apoptosis achieved by nanomaterial induced ROS generation.[14,37]

Antibacterial therapy lacks anti-inflammation, as the ROS mediated antibacterial operation is likely to be pro-inflammatory.

[a]*School of Materials Science and Nanotechnology, Jadavpur University, Kolkata-700032, India. E-mail: chandu_ju@yahoo.co.in*

[b]*Department of Electronics and Telecommunication Engineering, C V Raman Global University, Mahura, Khorda, Orissa-752054, India*

[c]*School of Bioscience and Biomedical Engineering, Jadavpur University, Kolkata-700032, India*

[d]*Institute for Science and Technology in Medicine, School of Medicine, Keele University, Stoke-on-Trent, ST4 6QG, UK*

[e]*Department of Biomedical and Life Sciences, Lancaster University, Lancaster, LA1 4YG, UK*

[f]*Department of Chemistry, Lancaster University, Lancaster, Lancashire LA1 4YB, UK. E-mail: j.g.hardy@lancaster.ac.uk*

[g]*Materials Science Institute, Lancaster University, Lancaster, Lancashire LA1 4YB, UK*

† Electronic supplementary information (ESI) available. See DOI: 10.1039/d0ra01129k

Investigating the anti-oxidant properties of such nanomaterials towards macrophages is of interest, because macrophage targeting may be an effective strategy to deliver anti-inflammatory drugs to sites of inflammation.[38] Inflammation (a localized swelling, pain, redness due to some injury or infection) is promoted by several mechanisms including ROS generation in macrophages.[39] Studies on nanoparticle induced anti-inflammatory activity in macrophages suggest inflammation is activated by extracellular matrix protein, lipopolysaccharides (LPS) and cytokines.[38] The size of nanoparticles facilitates their uptake by macrophages.[38] *In vitro* studies on the anti-inflammatory activity of RAW 264.7 macrophages by nanoparticles (*e.g.* PLA-PEG, Prussian blue nanoparticles),[40,41] and *in vivo* studies using biogenic Ag nanoparticles (NPs) demonstrated that the NPs exhibited simultaneous antimicrobial and anti-inflammation activity,[42] *via* various anti-inflammatory pathways.[43] Despite the literature on metal oxide nanoparticle induced anti-inflammatory activity[38,39] there is little literature on the anti-inflammatory effects of nanoparticles in the light/dark. Materials with simultaneous antibacterial and anti-inflammation activity have potential for a variety of biomedical applications.

Polymers displaying antimicrobial properties are the subject of significant attention for their potential technical and medical applications.[44–49] Polyindoles have excellent thermal stabilities (important for sterilization, *e.g.* in an autoclave) and redox activities and therefore have potential for application as antibacterial materials.[48–50] Ag_3PO_4 displays visible light induced antibacterial activity,[51] albeit concomitant with photodegration.[52] The valence band edge potential of Ag_3PO_4 (E_{VB} = 2.66 eV) is greater than E_H of $\cdot OH/H_2O$ (2.2 eV) which makes it a potent source of $\cdot OH$ radicals, which has been shown to result in antibacterial activity.[16] The composites reported here also show radical induced antibacterial activity. Pln was chosen to stabilise the nanocomposite as Ag_3PO_4 is structurally unstable when it is dissolved in water.[53] Pln is a chemically and thermally stable polymer[48] which can inhibit Ag_3PO_4 decomposition, moreover, its valence band edge potential (E_{VB} = 3.45 eV) can induce elevated $\cdot OH$ which inhibits bacterial population.

Herein we report the results of our studies on the structure and properties of Ag_3PO_4/polyindole composites and their antibacterial activity towards Gram positive *S. aureus* and Gram negative *E. coli* at different points in time (1, 2, 5 and 7 days in culture). The antibiofilm activity of the nanocomposites was explored in the dark. The intra-cellular ROS generation and bacterial cell membrane disintegration were monitored using 2′,7′-dichlorofluorescein diacetate (DCFH-DA) and propidium iodide (PI) dye respectively. Furthermore, we explored the application of the nanocomposites in MCF-7 breast cancer cells to understand their potential for use in ROS mediated cancer therapy. Finally, we examined the anti-inflammatory activity of the nanocomposites towards human monocyte THP-1 derived macrophages to understand the radical scavenging behaviour. The broad spectrum of interesting properties displayed by such nanocomposites offer them opportunities for a multitude of biomedical applications.

Experimental

Materials and methods

Silver nitrate ($AgNO_3$), sodium chloride (NaCl), potassium chloride (KCl), potassium dihydrogen phosphate (KH_2PO_4) were supplied by Merck, India. Indole (C_7H_8N, 99%), ammonium persulphate ($(NH_4)_2 \cdot S_2O_8$, 98%), terephthalic acid (TA, $C_8H_6O_4$, 98%), 2′,7′-dichlorofluorescin diacetate (DCFH-DA, 97%), thiazol blue tetrazolium bromide (MTT) were supplied by Sigma Aldrich. Nitroblue tetrazolium chloride (NBT), propidium iodide (PI), nutrient broth (NB), nutrient agar (NA), crystal violet (CV), Furfuryl alcohol (FFA), Dulbecco's modified eagle's medium (DMEM), transparent 96 well-plates were supplied by Himedia, India. Black 96 well plates were obtained from Eppendorf AG, Germany. Fetal bovine serum (FBS) was procured from Gibco, L-Glutamine–Penicillin–Streptomycin was purchased from Central Drug House Fine Chemicals, Delhi, India. Ethanol was supplied by Merck, Germany. 0.45 μm filter paper was supplied by Whatman. Roswell Park Memorial Institute (RPMI) 1640 was obtained from Lonza Bio-Whittaker™. The THP-1 peripheral blood acute leukaemia cell line was purchased at passage 2 from Sigma-Aldrich (88081201, USA). 1,1-Diphenyl-2-picrylhydrazyl radical (DPPH), HEPES, sodium pyruvate, phorbol 12-myristate 12-acetate (PMA), and lipopolysaccharide (LPS) were supplied by Sigma Aldrich (Gillingham, UK). IFN-γ and recombinant human macrophage colony stimulating factor (M-CSF) were purchased from Pepro-Tech, USA. MCF-7 breast cancer cell lines were obtained from NCCS, Pune, India. Both Gram-positive *S. aureus* (ATCC 29737) and Gram-negative *E. coli* (ATCC K88) were purchased from ATCC. Unless otherwise noted, all reagents were used without any further purification.

Synthesis of Ag_3PO_4

Ag_3PO_4 nanocrystals were prepared according to the literature with some minor modifications.[53] Briefly, $AgNO_3$ (0.4 g) was added to distilled (DI) water (20 mL) and stirred for 15 min after which an aqueous solution of Na_2HPO_4 (0.284 g in 20 mL DI water) was added dropwise and the mixture was stirred for 5 h. The yellow precipitate was isolated by centrifugation and washing repeatedly with DI water and ethanol (until the liquid was clear and colourless) after which it was dried under vacuum at 55 °C for 24 h to obtain Ag_3PO_4 nanocrystals.

Synthesis of polyindole (Pln)

Polyindole was synthesized by ammonium persulfate initiated polymerisation of indole using a process reported in the literature.[54] The as synthesized polyindole is hereafter referred to as Pln0.

Preparation of Ag_3PO_4/polyindole composites

Ag_3PO_4/polyindole composites were prepared by *in situ* growth of Ag_3PO_4 nanocrystals inside a matrix of polyindole by adaptation of the literature.[55] As synthesized Pln0 (0.1 g) was dispersed in DI water (25 mL) and sonicated for 5 min. A certain

amount of $AgNO_3$, which was decided by the weight percentage of PIn in the PIn/Ag_3PO_4 composite, was added into this mixture and the liquid mixture was stirred for 1 h. A certain amount of Na_2HPO_4, which is equal to 33.33% (in mole percentage) of the added $AgNO_3$ in the liquid mixture, was dissolved in 25 mL deionized water. The prepared Na_2HPO_4 solution was then slowly added dropwise into the stirred mixture of PIn and $AgNO_3$. The suspension was stirred for 5 h. The mixture was centrifuged and washed with anhydrous ethanol and DI water repeatedly until the liquid was clear and colourless, after which the composites were dried under vacuum at 55 °C for 24 h. The amount of $AgNO_3$ present in the composites was quantified using a high precision balance and recording the mass of starting polyindole (0.1 g) and mass of the composite after washing and drying. Ag_3PO_4/Pln composites with mass ratios of 4 : 1, 2 : 1, and 1 : 1 (w/w) were designated as Pln1, Pln2 and Pln3, respectively.

Characterization

The crystallinity and phase of the samples were characterized by X-ray diffraction (XRD) (Ultima-III, Rigaku, Japan). The size and morphology of the samples were characterized by scanning electron microscopy (SEM) and transmission electron microscopy (TEM). SEM images were obtained using a JEOL JSM 7800F scanning electron microscope (JEOL, Welwyn Garden City, UK).For qualitative EDX analysis, the samples were sputter coated with a layer of gold (60 s, 20 mA, 8×10^{-2} mBar, *ca.* 5 nm) using a Quorum Q150RES sputter coater (Quorum Technologies Ltd) and then investigated using a field-emission SEM JEOL JSM 7800F with an energy dispersive X-ray spectroscopy (EDX) system (X-Max50, Oxford Instruments, Abingdon, UK) at 10 mm working distance and 10 kV voltage mounted on a brass JEOL holder with 25 mm carbon tabs (G3348N, Agar Scientific, Stansted, UK). Three measurements were performed per sample and average results are presented. TEM images were obtained for the samples collected onto 400 mesh formvar carbon grids (Agar Scientific, UK) in a JEOL 10–10 TEM at 80 kV images acquired with an AMT NanoSprint500 (Deben, UK). Fourier transform infrared (FTIR) spectra of the samples were obtained using an IR Prestige (Shimadzu, Japan) in absorbance mode. Diffused reflectance spectroscopy was conducted using a UV-Vis spectrophotometer (Shimadzu, Japan), and ζ potential was measured using a Zetasizer NS Nano, zeta analyser (Malvern Panalytical Ltd, Malvern, UK).

Antibacterial activity measurement

The antibacterial activity of Ag_3PO_4/Pln nanocomposites was evaluated by minimum inhibitory concentration (MIC) tests and turbidity methods against Gram-positive bacteria *S. aureus* and Gram-negative bacteria *E. coli*. MIC evaluation was carried out by agar dilution method.[56] Specifically the nanocomposites were dissolved in DMSO (2%) and sterile water to make the final concentration of 2000 μg mL^{-1} which was further diluted to 0.5, 1, 5, 10, 20, 40, 100, 200, 400, 600, 800, 1000 μg mL^{-1}. Each inoculum (2×10^6 CFU mL^{-1}) was spotted in agar plates containing those concentrations and incubated at 37 °C for 24 h. Minimum concentration of the drug that inhibits bacterial growth was recorded as MIC. For turbidity measurements 200 μL of the nanocomposite solutions were added to 1 mL of fresh inoculums (~1.5×10^8 CFU mL^{-1}) in 2 mL Eppendorf tubes and incubated at 37 °C for 24 h in an orbital shaker (150 rpm). Bacteria without nanocomposites were used as control. The absorbance of bacterial suspension was recorded using UV-Vis spectrophotometer (JASCO V650) at 600 nm. The antibacterial potency was expressed as change in absorbance at 600 nm.[57]

$$\% \text{ Inhibition} = \frac{OD_{control} - OD_{sample}}{OD_{control}} \times 100 \quad (1)$$

The antibacterial activity tests were performed in triplicate.

Anti-biofilm activity measurement

Biofilm inhibition of *S. aureus* and *E. coli* was quantified by a colorimetric detection process.[6,16,58] Specifically, fresh inoculums (1×10^6 CFU mL^{-1}, 200 μL) was pipette out white 96 well-plate onto which the nanocomposite solutions (1g L^{-1}) were added and incubated at 37 °C for 4 days. Control wells were marked without the nanomaterials. Each incubated well was rinsed thrice with sterile distilled water to remove any free bacteria. CV (10% (v/v), 400 μL) was pipetted out of each well and left for 1 h to stain the biofilm followed by washing with sterile distilled water. Quantification of biofilm was assessed by eluting CV with 95% ethanol (400 μL) for 10 min. Finally, the mixture (200 μL) was pipetted out into another transparent 96-well plate and the absorbance was recorded at 570 nm by UV-Vis spectrophotometer (SpectraMax M5, Molecular Devices). Biofilm inhibition was expressed as change in absorbance at 570 nm and calculated as:

$$\% \text{ Inhibition} = \frac{A_{control} - A_{sample}}{A_{control}} \times 100 \quad (2)$$

In vitro reactive oxygen species detection

The *in vitro* study of reactive oxygen species (ROS) generation from Ag_3PO_4/Pln nanocomposites was conducted by measuring the generation of superoxide anion ($O_2^{\bullet -}$) and hydroxyl radical ($\cdot$OH) as previously reported by our group.[57] Typically for $O_2^{\bullet -}$ generation, each sample (1000 μg mL^{-1}) was added into NBT (1 mM) solution with vigorous stirring in the dark for 24 h. The reaction product was then subjected to centrifugation (5000 rpm, 10 min) and filtration after which the aliquots (3 mL) were collected and the absorbance was recorded with an UV-Vis spectrophotometer (JASCO V650) at 259 nm using quartz cuvettes with 1 cm path length.

For $\cdot$OH generation, TA (2 mM) was added to an aqueous suspension of each of the nanocomposite with their bare counterparts (1000 μg mL^{-1}) with vigorous stirring in the dark for 24 h. The reaction product (5 mL) was subjected to centrifugation (5000 rpm, 10 min) and successive filtration (Whatman, 0.45 μm) and 200 μL of the supernatant was transferred into black 96-well plates. The fluorescence intensity (λ_{ex} 312 nm/λ_{em} 430 nm) was measured with a fluorescence plate reader (SpectraMax M5, Molecular devices).

For $^1O_2$ generation, FFA (0.85 mM) was added to an aqueous suspension of each of the nanocomposite with their bare counterparts (1000 μg mL^{-1}) with vigorous stirring in the dark for 24 h. The reaction product (5 mL) was subjected to centrifugation (5000 rpm, 10 min) and successive filtration (Whatman, 0.45 μm). The aliquots (3 mL) were collected and the absorbance was recorded with a UV-Vis spectrophotometer (JASCO V650) at 217 nm using quartz cuvettes with 1 cm path length.

Intra-cellular ROS detection

Intra-cellular ROS detection for Ag_3PO_4/Pln nanocomposite was carried out by minor adaptation of the literature.[59] In a typical process, Gram positive bacteria *S. aureus* and *E. coli* were freshly grown up to log phase ($OD_{600} = 0.2$ corresponding to 10^8 CFU mL^{-1}) in Nutrient broth (NB). The grown bacteria were treated with 1g L^{-1} of Ag_3PO_4, Pln0, Pln1, Pln2 and Pln3 for 1 h, centrifuged at 8000 rpm for 5 min and suspended in saline (0.8 g L^{-1} NaCl, 0.2g L^{-1} KCl). Bacteria without nanomaterials were used as controls. 2,7-Dichlorodihydrofluorescein diacetate (DCFH-DA), a fluorescence probe was added to each of specimens and incubated for 3 h at ambient temperature in the dark. The fluorescence of each sample was then measured by fluorescence plate reader (Spectra Max M5, Molecular device) with excitation and emission wavelengths of 485 nm and 530 nm respectively.

Membrane integrity test

Permeability of the inner bacterial membrane was studied with a membrane-impermeable fluorescent dye, PI (Propidium iodide).[60] Freshly prepared *S. aureus* and *E. coli* were diluted to $OD_{600} = 0.05$, centrifuged at 8000 rpm for 5 min and suspended in PBS buffer. A stock solution of PI (3 mM in sterilised water) was diluted 10^3-fold of which 2 μL was added to bacterial suspension. 1 g mL^{-1} of Ag_3PO_4, Pln0, Pln1, Pln2 and Pln3 were added to the PI containing bacterial suspension and kept for 15 min in 96 well plate. The fluorescence intensity was measured with a fluorescence plate reader (SpectraMax M5, Molecular Device) at 25 °C with excitation and emission wavelengths of 540 and 610 nm, respectively.

Cytotoxicity determination assay

To evaluate the cytotoxicity of the Ag_3PO_4/Pln nanocomposites against different mammalian cells. The cytotoxicity of the materials was evaluated using a MTT assay against Peripheral Blood Mononuclear cells (PBMC) and MCF-7 breast cancer cells to determine cell metabolic activity.[59,61] After attainment of 70% confluence the cells were seeded in 96 well plates at a density of 0.3×10^4 cells per well after which they were treated with materials at different concentrations and incubated at 37 °C with 5% CO_2 atmosphere for 24 h. After 24 h of incubation, MTT at 5 mg mL^{-1} is transferred to each well and the whole system is incubated for 3 h at 37 °C. The incubation is terminated by recording the absorbance of cells at 590 nm using a UV-Vis Spectrophotometer (Version 2.00, Agilent Technologies Cary 60). All experiments were carried out in triplicate and the results are obtained reported as the mean ± standard deviation.

Cell culture

PBMC isolation and culture. A density gradient separation method was employed to isolate the human PBMCs. Ethical permission for blood collection was granted by the Institutional Bio-Ethics committee, Jadavpur University (letter dated 24.03.2017 against application dated 21st December, 2016). Typically, 3 mL of the human blood was mixed with anticoagulant agent EDTA after collected from a healthy donor with his/her consent. The as collected blood was thereafter diluted to 1 : 3 ratio with chilled saline (0.9%) out of which 7.5 mL of the diluted blood was added to 2.5 mL of Lymphoprep (Fresenius Kabi Norge AS) in order to develop a density gradient solution. Subsequently the blood was centrifuged at 5000 rpm for 30 min in order to filter the mononuclear cells that appear as white rings. The cells are subsequently washed with PBS and serum free RPMI-1640 medium and suspended in RPMI 1640 medium supplemented with 10% Fetal Bovine Serum (FBS) and 1% penicillin–streptomycin. Finally, the cells were maintained in a humidified incubator with 5% CO_2 at 37 °C.

MCF-7 breast cancer cell culture. MCF-7 breast cancer cell lines were freshly prepared as per standard animal cell culture laboratory protocol.[59] Typically the cells were grown in DMEM supplemented with 10% FBS, 100 U mL^{-1} penicillin and 100 μg mL^{-1} streptomycin. The cells were thereafter maintained at 37 °C in a humidified incubator with 5% CO_2. When 70% confluence is arrived the cells were washed with DMEM twice and incubated with nanomaterial in a 96 well plate.

***In vitro* anti-oxidation measurement.** The anti-oxidation activity of nanomaterials was determined by the free radical scavenging capacity of the nanomaterials. The nanocomposites were prepared at a concentration of 1 mg mL^{-1} in methanol and homogenized in an ultrasonic bath (FB11201, Fisherbrand) for 20 minutes. The DPPH free radical was made at 0.1 mM in methanol, and mixed with the nanocomposite suspension in a ratio of 300 μL : 100 μL. The mixed solution was then homogenized by vortex for 20 seconds and cultured at room temperature for 30 minutes. Solutions were filtered after incubation and read by a plate reader (BioTek) at 517 nm, with methanol as control.

***In vitro* anti-inflammation study.** THP-1 cells were cultured in RPMI 1640 supplement with 10% FBS, 1% penicillin–streptomycin, 10 mM HEPES and 1 mM sodium pyruvate. THP-1 cells were seeded in Corning® 96 well plates at a density of 2×10^4 cells per well with the inducing media that consisted of 100 ng mL^{-1} PMA and 100 ng mL^{-1} of M-CSF, and cultured for 48 h. After that, the THP-1 derived macrophages were refreshed with fresh culture media with 1 μg mL^{-1} LPS, IFN-γ and each type of particles at a ratio of 50 particles per cell. The cell culture media was collected after 18 h culture in the dark, and mixed with the Griess reagent solution (1% sulfanilamide, and 0.1% naphthalene diamine dihydrochloride in 2.5% phosphoric acid) at a ratio of 50 μL : 50 μL. The mixture was incubated at room

temperature for 10 minutes and read by a plate reader (BioTek) at 540 nm.

Results and discussion

Nanocomposite characterization

Fig. S1A† depicts the XRD pattern of the investigated samples. Fifteen diffraction peaks corresponding to $2\theta = 20.85°$, 29.70°, 33.30°, 36.55°, 42.50°, 47.79°, 52.7°, 55.00°, 57.29°, 61.64°, 69.95°, 71.90°, 73.85°, 87.25°, 89.15° were identified for all the samples. They were readily indexed as (110), (200), (210), (211), (220), (310), (222), (320), (321), (400), (420), (421), (332), (520), (521) planes of body centred cubic structures of Ag_3PO_4 (JCPDS file no. PDF # 06-0505). The absence of any other peak validated the phase purity of the synthesized composites.[52] The average crystallite size was calculated from the Debye–Scherrer relation:

$$D = \frac{0.9\lambda}{\beta \cos \theta} \quad (3)$$

where D is the crystallite size, $\lambda = 1.5406$ Å, and θ and β represent the Bragg's diffraction angle and FWHM respectively. The broad diffraction pattern around $2\theta = 20.3$–$26.9°$ was attributed to formation of pure polyindole (Pln0).[48] It is interesting to note that the pattern did not vary in peaks in case of Pln1, Pln2 and Pln3 which indicated unaffected crystal structure of Ag_3PO_4 particles inside the matrix of Pln or on its surface. In these samples, no characteristic peaks of Pln were detected implying coating of Ag_3PO_4 by amorphous Pln.[48] The formation of Ag_3PO_4/Pln composite was further confirmed by FTIR spectra (Fig. S1B†). An intense peak at 744 cm^{-1} related to C–H of Pln was diminished from Pln3 to Pln1 (ref. 48) (Fig. S1B–D†). The strong peak at 1102 cm^{-1} corresponding to the C–N of Pln0 (ref. 48) also decreased in intensity from Pln3 to Pln1. Similarly the C–N and C=C (stretching) peaks of Pln0 observed at 1456 cm^{-1} and 1613 cm^{-1}, respectively,[48] diminished from Pln to Pln3 to Pln1. The presence of Ag_3PO_4 in all composites was further affirmed from presence of characteristic peaks at 561 cm^{-1} and 1011 cm^{-1} which corresponded to asymmetric bending and asymmetric stretching of P–O bonds of pristine Ag_3PO_4.[62] Interestingly the intensity of these peaks was lower in Pln3 and Pln2 as compared to Pln1 implying that decreasing Ag_3PO_4 proportion from Pln1 to Pln3. Peaks at 1388 cm^{-1}, 1679 cm^{-1} and 3120 cm^{-1} of pristine Ag_3PO_4 corresponded to antisymmetric stretching mode of the PO_4^{3-} group, and the bending vibration of H–O–H and stretching vibration of O–H group due to water molecules adsorbed on the surface respectively.[62] These peaks almost disappear and blue shifted in Pln2 and Pln3 implying some of the Ag_3PO_4 was buried inside the Pln matrix.[63]

Fig. S2† depicts characteristic SEM images of pristine Ag_3PO_4, Pln0 and their composites. Pre Ag_3PO_4 particles were observed to agglomerate; Pln0 particles were mostly spherical, whereas the composites appeared to be spherical particles with Ag_3PO_4 particles visible on the surfaces. EDX data supported the proposed elemental compositions (*i.e.* Ag, P and O for the Ag_3PO_4, C, N, O for the polyindole Pin0, and a mixture of these for the composites). The TEM results (Fig. S3A–F†) correlated with the FESEM results for the samples of Pln0, Pln1, Pln2 and Pln3; showing agglomerates of mostly spherical and oblate shaped particles with some angular particles visible. When examined under extreme magnification the TEM images suggest that the Ag_3PO_4 material was heterogeneous with approximately 10 nm sized internal inclusions visible (Fig. S3B†). Importantly, for the composites, the TEM images show there to be Ag_3PO_4, embedded in the PIn particles (*i.e.* not only on the surface).

The band gap energy (E_g) of pure Ag_3PO_4, Pln0 and their composites were characterized by diffused reflectance spectroscopy (Fig. S4†) and the respective values were 2.39, 2.46, 2.36, 2.42 and 2.33 eV as estimated by the Kubelka–Munk (K–M) function.[62] The band gap values of pure Ag_3PO_4 and Pln could facilitate generation of ·OH but no $O_2^{\bullet -}$ due to the band edge energy. The band edge energy was calculated using the electronegativity and E_g:[56,64]

$$E_{VB} = \chi - E_e + \frac{1}{2}E_g \quad (4)$$

$$E_{CB} = E_{VB} - E_g \quad (5)$$

where E_{VB} and E_{CB} are the conduction and valence band edge potential, χ is the Mulliken electronegativity,[65] E_e is the free electron energy on the hydrogen scale (4.5 eV)[66] and E_g is the band gap of material.

According to the above-mentioned relation the E_{VB} and E_{CB} of pure Ag_3PO_4 ($\chi = 5.96$ eV) and Pln0 ($\chi = 6.717$ eV) were 2.66, 0.27 eV and 3.45, 0.99 eV in NHE scale respectively. The redox potential (E_H) of $O_2^{\bullet -}/O_2$ and ·OH/H_2O were −0.2 eV and 2.2 eV respectively[67] thus Ag_3PO_4 and Pln0 both could not be capable to generate $O_2^{\bullet -}$ in conduction band ($E_{CB} > E_H\ O_2^{\bullet -}/O_2$) but ·OH can be yielded from their valence band ($E_{VB} > E_H$ ·OH/H_2O) accordingly. Additionally E_H of $^1O_2/O_2$ is 1.8 eV in NHE scale[67] thus Ag_3PO_4 and Pln0 can yield $^1O_2$ as their E_{VB} were greater than the prescribed value.

Study of long term antibacterial activity

Metal oxide nanoparticles and their composites were established as potent antibacterial agents[8,16] due to defect induced ROS generation and their respective oxidative stress but their antibacterial activity is observed to deteriorate after prolonged exposure.[54] Interestingly in this present work we have demonstrated antibacterial activity of Ag_3PO_4/polyindole composites after prolonged exposure for 1–7 days. For this purpose Ag_3PO_4/polyindole nanocomposite were exposed to two of the most common pathogenic bacteria including Gram-positive *S. aureus* and Gram-negative *E. coli*. Initially we have investigated MIC of each type of nanocomposite (shown in Table 1).

The MIC values of the Ag_3PO_4/polyindole composite was found to be comparable with that of other metal oxide nanoparticles.[9,68,69] Interestingly, the Ag_3PO_4/polyindole nanocomposites extraordinarily exhibit growth inhibition property against both bacteria whereas Pln0 does not exhibit any antibacterial activity at this concentration range. Observations reveal that Pln1, Pln2 and Pln3 were more sensitive to both

Table 1 Minimum inhibitory concentration (MIC) value of pristine Ag_3PO_4, Pln0, Pln1, Pln2 and Pln3

	MIC (μg mL^{-1})	
Sample	*E. coli*	*S. aureus*
Ag_3PO_4	5.0	20.0
Pln0	Not found	Not found
Pln1	0.5	5.0
Pln2	0.5	5.0
Pln3	0.5	5.0

bacteria as compared to bare Ag_3PO_4 implying a synergistic effect of the nanocomposites. Additionally the sensitivity of all samples was more to *E. coli* than *S. aureus*. This behaviour suggested a physiological difference between these two bacterial strains. *S. aureus* has a thicker peptidoglycan layer at its cell wall as compared to *E. coli* so it may be easier for the nanocomposite to diffuse into the cell wall of *E. coli* than *S. aureus* but such an event can only be possible if there is close contact between nanomaterial and bacteria. This proximity was a resultant phenomenon due to electrostatic attraction between nanomaterials and bacteria due to the surface charge of both entities. Fig. S5† depicts the zeta potential of Ag_3PO_4/Pln nanocomposite along with their bare forms. From Fig. S5† it was observed that all nanomaterials had a highly negative surface charge especially Pln3 which renders the close proximity of the nanomaterials and bacteria less likely as the surface charge of *E. coli* and *S. aureus* were −47 mV and −38 mV respectively.[70] The data presented in Table 1 showing the excellent bacterial sensitivity of the nanocomposites suggested other phenomenological events influence the MIC. Based on the MIC result and our motivation to study the prolonged antibacterial activity measurements we have investigated bacterial interactions with nanocomposites after 24 h, 48 h, 120 h and 168 h (7 days) using a turbidity method[16] produced a more accurate result against *S. aureus* and *E. coli*. (shown in Fig. 1A–D), from which it was evident that the untreated *E. coli* (CNTRL-N) exhibited exponential growth up to 24 h and started decaying after that. The optical density (OD_{600}) of *E. coli* with Pln0 and Pln1 was found to follow the pattern similar to CNTRL-N with lower OD implying inhibition of bacterial growth over the duration of the experiment and Pln1 substantially inhibited *E. coli* to a greater extent than Pln0 (Fig. 1A). The OD pattern of Pln2 and Pln3 was highly suppressed compared to CNTRL-N implying bactericidal activity. Pure Ag_3PO_4 initially followed a similar turbidity pattern as that of Pln3 but experienced a sudden rise in turbidity after 48 h. This unperturbed increment of OD in presence of Ag_3PO_4 may be due to the degradation of Ag_3PO_4.[53]

In the case of *S. aureus*, the untreated solution (CNTRL-P) exhibited exponential growth to 24 h and became saturated for the rest of the experiment. Further observation revealed that Pln1, Pln2 and Pln3 followed similar OD patterns as that of CNTRL-P, but with suppressed intensity implying bacteriostatic activity.[16] Among them Pln1 caused lowest turbidity of *S. aureus*

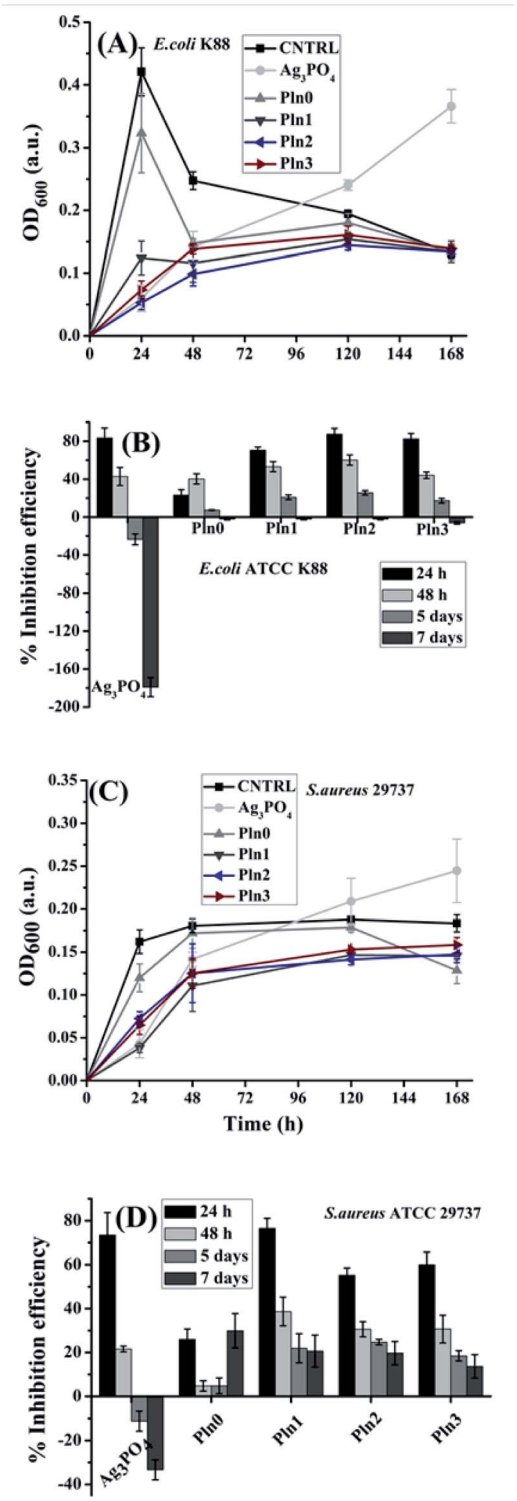

Fig. 1 (A and B) Growth kinetics of *E. coli* and *S. aureus* in the presence of pure Ag_3PO_4, Pln0 and Ag_3PO_4/polyindole composites in the dark respectively. (C and D) % inhibition efficiency of *E. coli* and *S. aureus* after incubation with pure Ag_3PO_4, Pln0 and Ag_3PO_4/polyindole nanocomposites for different time periods respectively. CNTRL is untreated bacteria as a control.

solution among all samples indicating its highest antibacterial propensity. In the case of Pln0, the antibacterial activity was sustained for 7 days. Ag_3PO_4 initiated bacterial interactions

with inhibitions as observed from its OD pattern (Fig. 1B), but after 48 h there was a gradual increase in the OD implying strong repulsive interaction with *S. aureus*. The antibacterial activity of polyindole composites over prolonged exposure was particularly interesting. Fig. 1C and D explores the percentage inhibition efficiency of composites for 7 days against both bacteria. Pure Ag_3PO_4 exhibited 83.4 and 73.5% inhibition efficiency against *E. coli* and *S. aureus* respectively after 24 h and this efficacy gradually diminished as time surpasses and attains negligible value after 7 days. Pln0 exhibited moderate antibacterial activity, *e.g.* 23.2 and 26.0% against *E. coli* and *S. aureus* after 24 h respectively and it was noteworthy that after 5 days the inhibition efficiency is 7.4 and 4.8% against *E. coli* and *S. aureus*, respectively, *i.e.* long-term antibacterial activity. Pln1 displayed higher antibacterial activity (70.5, 76.5% and 20.8, 22.0% efficiency against *E. coli* and *S. aureus* after 24 h and 5 days respectively) than Pln0. Pln2 inhibited the growth of *E. coli* and *S. aureus* by 87.4 and 55.3% after 24 h, respectively. It is noteworthy that the highest antibacterial activity was achieved by Pln2 against both bacteria after 5 days (25.6 and 24.8% against *E. coli* and *S. aureus*, respectively). Similar bacterial growth inhibition pattern was observed for Pln3. By synthesizing Ag_3PO_4/polyindole composites at 2 : 1 w/w ratio, we have achieved two goals simultaneously in: superior antibacterial activity and sustained bacterial inhibition for a prolonged time. Long term interaction with *S. aureus* was more effective than for *E. coli* (Fig. 1C and D). After 7 days exposure it was observed that all composites exhibited higher antibacterial activity against *S. aureus* than *E. coli*.

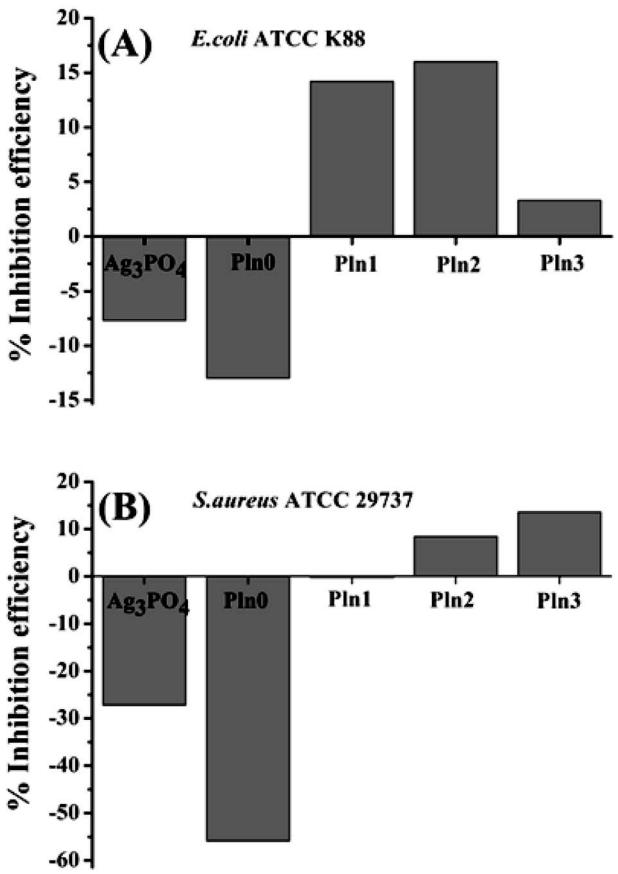

Fig. 2 (A and B) Biofilm inhibition efficiency against *E. coli* and *S. aureus* after 4 days exposure of pure Ag_3PO_4, Pln0 and Ag_3PO_4/polyindole nanocomposites.

Biofilm inhibition

In nature, bacteria other than its planktonic forms sometimes build up aggregated and stacked layers of surface-adherent structured communities known as biofilms, which sometimes present resistance to bioactive molecules (particularly antibiotics). Several mechanisms were proposed for this resistance against antibiotics, including primarily adhesion of bacteria to living and non-living surfaces which resist *in vivo* any host immune systems or biocides and undertake cellular processes at relatively slower rates in order to be antibiotic resistant.[71] Moreover, a biofilm's exopolymeric matrix and bacterial dead cells act as a barrier for the diffusion of antibiotics/drug molecules thus protecting the live bacteria.[72] Therefore the design and development of novel biofilm inhibitors is a societal grand challenge. Ag_3PO_4/Pln composites and the constituent materials alone can be delivered to biofilms formed by *E. coli* and *S. aureus* as these biofilms were frequently found in orthopaedic implant devices.[68]

The anti-biofilm activity of the materials was measured using a crystal violet assay based colorimetric detection protocol (Fig. 2A and B) which in advance quantifies the amount of extracellular polymeric substances, generated by biofilms and indirectly monitors biofilm biomasses.[6,16,58] The respective inhibition efficiency of these nanocomposites is calculated according to the method suggested by Jaiswal *et al.*[73] It is noteworthy that the Ag_3PO_4/Pln nanocomposites inactivate the microbial biofilms to various extents. The highest biofilm inhibition efficiency against *E. coli* was observed for Pln2, followed by Pln1 and Pln3 (Fig. 2A). Similarly for *S. aureus* the highest inhibition was notified for Pln3 followed by Pln2 (Fig. 2B) Such an observation was comparable with that of Ag nanoparticles against *S. epidermis* (10–15%).[71]

Under the experimental conditions used, pure Ag_3PO_4 was unsuccessful at inhibiting bacterial biofilms which may be due to its structural instability.[53] Pln0 displayed long term antibacterial activity (Fig. 1C and D) but was unsuccessful in the retardation of biofilm formation (Fig. 2A and B). This can be ascertained from physiological differences between planktonic bacteria and their biofilms.[72] Therefore, simultaneous existence of antibacterial and anti-biofilm activity in Ag_3PO_4/Pln composites could enable them being efficient wound healing material especially for skin infection.[48] Interestingly, Pln2 exhibited the highest antibacterial and biofilm inhibition against *E. coli*, suggesting that these two activities were related with the electronic structure of Pln2 as well as its outcomes (*e.g.* ROS yield). Anti-biofilm activity is markedly less than the antibacterial activity, which was in line with the literature that materials with simultaneous antibacterial and anti-biofilm activity may not be efficient against mature biofilms.[73]

Antibacterial mechanism

The difference in antibacterial potency demonstrated earlier may be accounted for by the dissimilar cellular structures of *S. aureus* and *E. coli*, but the varied inhibition efficiency among composites indicated that parameters other than physiological differences between bacteria might be important. The means by which cellular damage by ROS[74] and non-ROS include the dissolution of cations,[7] internalization of nanostructures,[7] cell membrane disintegration *via* protein leakage,[75] membrane permeability changes[60] may explain the antibacterial activity of the nanostructured materials. We examined ROS generation from the nanostructures extracellularly and intracellularly.

In vitro ROS generation

ROS generated by semiconducting nanomaterials outside the cell are extracellular ROS. These free radicals are produced either by light irradiation or in the dark which essentially require two conditions: (1) the light energy should be greater or equal to the band gap of the nanomaterial and (2) defect states in nanomaterials which can facilitate electron transport.[76] In our present work we have carried out *in vitro* ROS generation assays in dark environments, so defect-induced electron transport is the accepted mechanism for ROS generation. Typically three different ROS′ are generated in semiconducting nanomaterials, superoxide anion ($O_2^{\bullet -}$), hydroxyl radical ($\cdot OH$) and singlet oxygen ($^1O_2$) as typically their generation involves conduction band electrons and valence band holes of nanomaterials. From *in vitro* ROS generation studies, we could not find any correlation between ROS yield with long-term antibacterial activity (Fig. S6†). Singlet oxygen can be formed due to valence band edge energy $E_{VB} = 2.66$ eV (>EH of $^1O_2/O_2 = 1.88$ eV) but there is no direct correlation between singlet oxygen generation with the antibacterial and anticancer activities, highlighting the need for further investigation. The different ROS generation abilities of Ag_3PO_4, Pln0, Pln1, Pln2 and Pln3 are related with mismatched band structure between silver phosphate and polyindole. Consequently, we employed an intracellular ROS generation assay to study antibacterial activity for long-term basis.

Intracellular ROS detection

High intracellular ROS levels and resultant oxidative assault have been highly cited as important factors for bacterial cell death induced by nanomaterials (including metal oxides and their polymer-based composites)[20] but long term intracellular ROS release and their impact on antibacterial activity of Ag_3PO_4/Pln nanocomposites was not reported elsewhere. We have presented such long-term release of intracellular ROS induced by Ag_3PO_4/Pln nanocomposites. During cellular metabolism, ROS are produced as by-products of biochemical reactions, $O_2^{\bullet -}$ is the primary ROS that is produced after O_2 consumption, and with the aid of dismutation reaction $O_2^{\bullet -}$ is transformed into H_2O_2 which is commonly known as intracellular ROS.[9,20,77] The ROS level is continuously being adjusted by endogenous antioxidants[77] but this ROS level might be increased by ROS′ produced under different environmental conditions by the nanomaterials.[76,77] To investigate the long-term potential of Ag_3PO_4/Pln nanocomposites to induce ROS generation in *E. coli* and *S. aureus*, DCFH-DA staining microplate assays were employed for 1–7 days. DCFH-DA is a cell permeable indicator for ROS and non-fluorescent dye until its acetate group is eliminated by cellular esterases during oxidation processes inside the cell. The intermediate reduced form of DCFH is subject to subsequent oxidation by H_2O_2 to produce dichlorofluorescein (DCF) which fluoresces. Thus, the fluorescent intensity of DCF indirectly measures the amount of H_2O_2 inside the cell. Fig. 3A and B depicts the intracellular H_2O_2 generation from *E. coli* and *S. aureus* after treatment with 1 mg mL^{-1} of nanocomposites for 1–7 days.

The intracellular ROS levels due to induction of nanocomposites was quite high but decayed over time. Pln2 induced the highest intracellular ROS in *E. coli*; whereas Pln3 did in *S. aureus* after treatment for 24 h., bare Ag_3PO_4 and Pln0 were incapable of inducing intracellular ROS levels in both bacteria after 24 h treatment. After 48 h of treatment, the nanocomposites (especially Pln2 and Pln1) induced high levels of intracellular ROS level in *E. coli* and *S. aureus* respectively. One noticeable finding was that the fluorescence intensities of *E. coli*

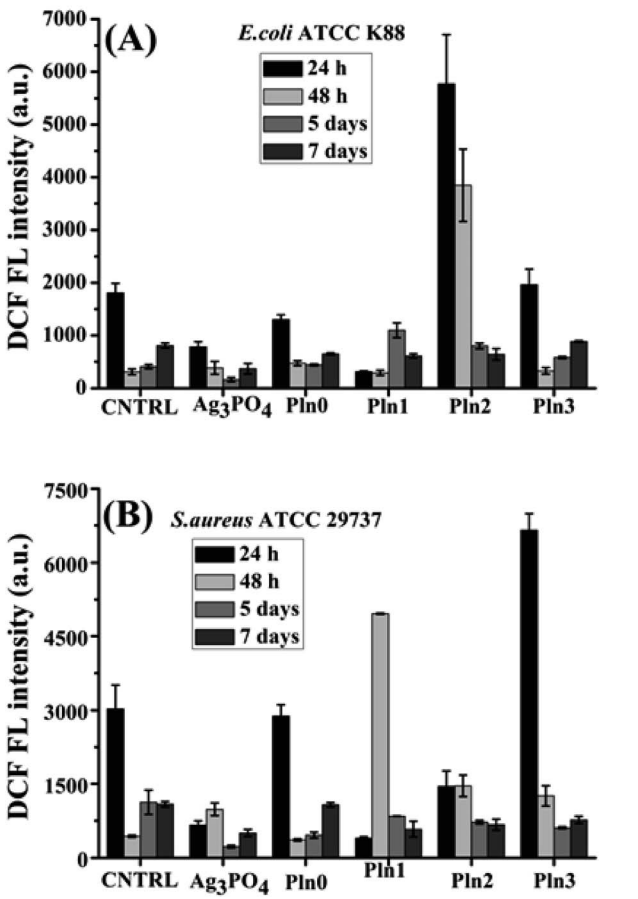

Fig. 3 Intracellular H_2O_2 generation form (A) *E. coli* and (B) *S. aureus* after treatment with Ag_3PO_4, Pln0, Pln1, Pln2 and Pln3 for 24, 48 h and 5, 7 days.

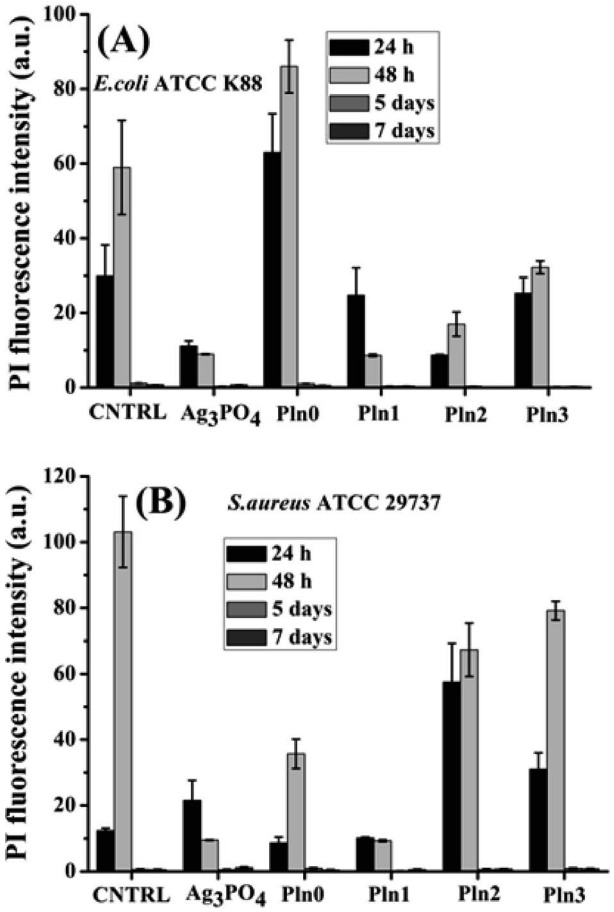

Fig. 4 FL intensity of PI in (A) *E. coli* and (B) *S. aureus* induced by Ag_3PO_4, Pln0, Pln1, Pln2 and Pln3 for 24, 48 h and 5, 7 days.

itself were drastically lowered from its 24 h value, which implies that the cells lack nutrients to grow and underwent degenerative processes, which further obstructed the cell permeation of DCFH-DA. Furthermore, the Ag_3PO_4/Pln nanocomposites induced ROS generation, corroborating their effect on antibacterial activity. The release of Ag^+ ions from the Ag_3PO_4 in the composite in the light exposure. As our investigation was carried out in the dark, there is less possibility of release of Ag^+ ions. Another observation was that although bare Ag_3PO_4 and Pln0 did not induce higher ROS levels in *E. coli* and *S. aureus*, their antibacterial activity (particularly after 24 h treatment) (Fig. 1C and D) require mechanistic studies of this antibacterial activity in the future. Targeting bacterial membrane functions is an emerging approach for inhibiting antibiotic resistant bacterial infections.[60] Unlike mammalian cell membrane, bacterial cell membrane is formulated by several negatively charged lipids *e.g.* cardiolipin, phosphatidylglycerol, lipopolysaccharides, lipoteichoic acid *etc.*[60] The basic mechanisms behind such membrane targeting include: binding the negatively charged membrane protein by cationic membrane active agents, and alteration of membrane permeability.[60] In our case the surface potentials of the Ag_3PO_4/Pln nanocomposites were anionic in nature so the binding force to membrane proteins was likely to be negligible so the antibacterial activity may be the outcome of membrane permeability alteration.

Membrane disintegrity measurement

In case of *E. coli*, high effect on cell permeabilization is observed only for Pln0 indicating bactericidal effect accounted to membrane disintegration (analogous to the literature).[60] A small effect on fluorescence was observed for Pln1 and Pln3 which provoked membrane depolarization for their antibacterial activity (Fig. 4). In the case of *S. aureus*, the membrane disintegration pattern (PI fluorescence) was also reproduced in Pln0, Pln2 and Pln3 while that of Pln1 resembles Ag_3PO_4 indicating sustainable membrane rupturing by Pln0 and its composites with increased polymer proportion and at the same time rapid degradation of Ag_3PO_4. Membrane permeabilization was most effective for Pln2 followed by Pln3 and Ag_3PO_4.

Cytotoxicity assessment of Ag_3PO_4/Pln nanocomposite

Ag_3PO_4/Pln nanocomposites have potential antibacterial ability in the dark by elevating levels of intracellular ROS. As ROS are important for killing cancer cells,[14,78,79] we have evaluated the anticancer activity of the Ag_3PO_4/Pln nanocomposites. The data presented in Fig. 5 demonstrates the activity of Ag_3PO_4/Pln nanocomposites in MCF-7 breast cancer cells treatment. The impact of Ag_3PO_4/Pln nanocomposites on the mortality of MCF-7 cells was assessed using the MTT assay. The cytotoxic effect of the nanocomposites on peripheral blood mononuclear cells (PBMCs) is depicted in Fig. 5A.

The results of the time and dose dependent study of the cytotoxic effect of the nanocomposites on MCF-7 cells is presented in Fig. 5B–F. From Fig. 5A it is observed that the nanocomposites became nontoxic to PBMC cells within 20–50 μg mL^{-1}, beyond which the composites showed toxicity towards the cell lines although the overall performance was still lower than cisplatin that exhibits 25% cell viability at 16.66 μg mL^{-1} after 24 h treatment. In the case of the MCF-7 cell line, cisplatin at this concentration showed 48 and 58% cell viability after 24 and 48 h treatment, respectively. To achieve anticancer activity with minimal damage of normal cells, Ag_3PO_4/Pln nanocomposites are under development. Due to the benign effect of Pln0, Ag_3PO_4 and Pln1 on PBMC cell lines; these materials have long-term potential for cancer treatment. The time dependent study of MCF-7 cells after treatment with Ag_3PO_4 showed 30% cell viability for 24 h and 40% for 48 h, if treated with 1 mg mL^{-1} but if we confined the treatment in the range of 20–50 μg mL^{-1}, bare Ag_3PO_4 exhibits negligible anticancer activity. Similarly, Pln0 also exhibited weak anticancer property over the entire concentration range. On the contrary Pln1 exhibits superior anticancer activity as compared to cisplatin, which is observed from 50–1000 μg mL^{-1}. It showed the highest anticancer activity with 24 and 26% cell viability after 24 and 48 h incubation if treated with 1 mg mL^{-1}. Even at lower concentration (20 μg mL^{-1}), Pln1 exhibited 59 and 54% cell viability after 24 and 48 h treatment. This result was comparable to that of fluorescein isothiocyanate (FITC)/ZnO nanocomposites as observed by

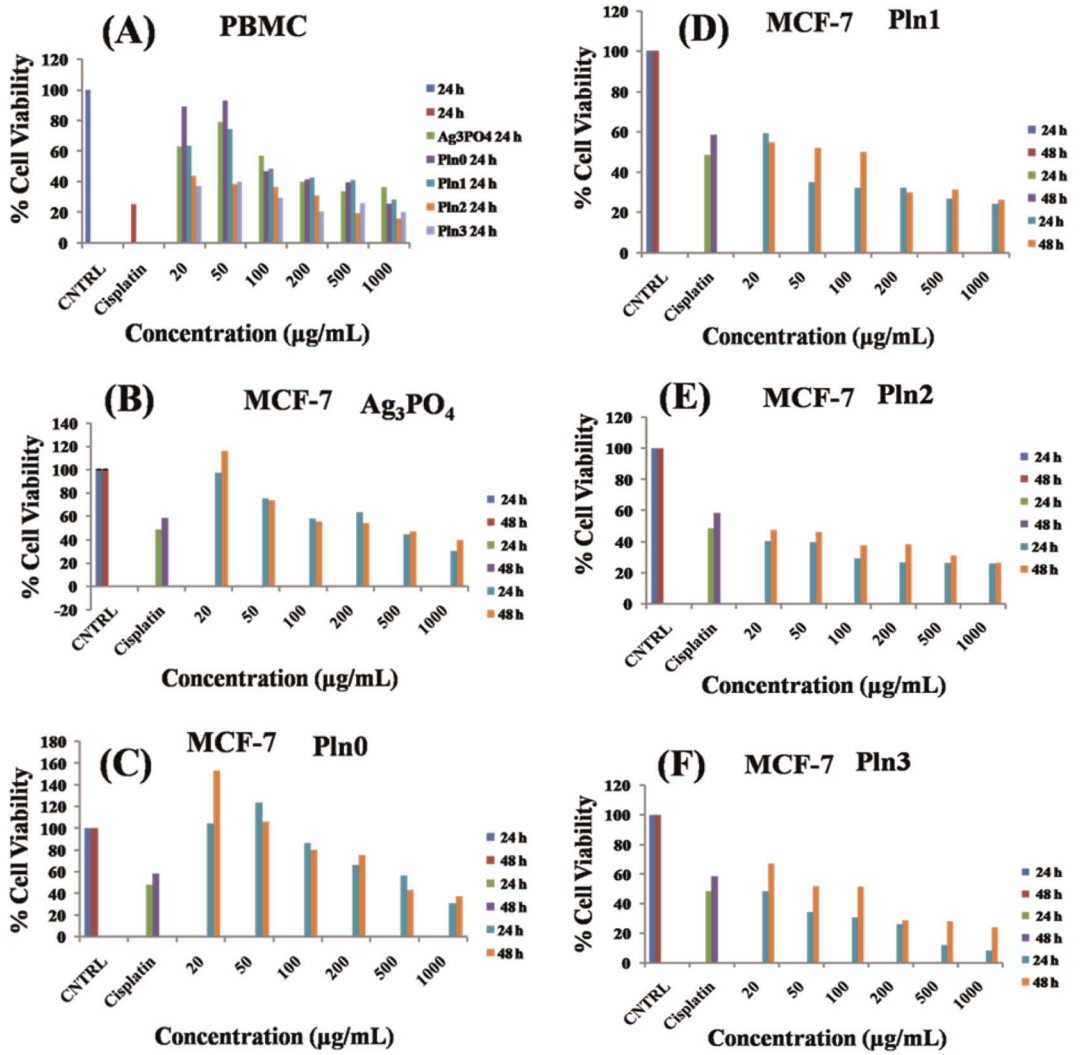

Fig. 5 (A) Cytotoxicity of Ag_3PO_4/Pln nanocomposite against PBMC cell after 24 h treatment, (B–F) cytotoxicity of Ag_3PO_4/Pln nanocomposite against breast cancer cell MCF-7 after 24 and 48 h treatment for comparative assessment.

Gupta *et al.*[14] This behaviour suggests potential long-term anticancer activity of Pln1. In the case of Pln2 and Pln3, excellent anticancer activity with minimal cell viability was observed, but due to considerable toxicity towards the PBMC cell, they are not employed in anticancer treatments as an alternative of cisplatin. Therefore, our cytotoxicity assessment demonstrates that these Ag_3PO_4/Pln nanocomposite can potentially inhibit cancer cell proliferation *in vitro* and may prove to be an alternative to conventional chemotherapeutic drugs.

In vitro anti-inflammation study

During bacterial infection macrophages are activated by lipopolysaccharides (LPS) which are components of the cell walls of Gram negative bacteria, and there is subsequent secretion of leukotrienes and pro-inflammatory cytokines like Tumor Necrosis Factor α (TNF-α) and Interleukin-1β (IL-1β).[38] Macrophages exposed to stimulants such as LPS or PMA experience respiration bursts which are further accompanied by ROS production resulting destruction of adjacent cells and tissues by the inflammation mechanism.[41] Therefore there is a need for the development of anti-inflammatory drugs to heal LPS induced macrophages. We used THP-1 derived macrophages as an *in vitro* model to investigate anti-inflammatory activity. The macrophages were initially treated by LPS and IFN-γ to understand the anti-oxidant nature of Ag_3PO_4/Pln nanocomposites (Fig. 6 and S7†). There was a dramatic change in morphology of the cells after incubation with LPS and IFN-γ (Fig. 6B). The cells were round in shape and bigger before the treatment (Fig. 6A), but after incubation with LPS and IFN-γ the cells become smaller and flatter with elongated shapes [Fig. 6B]. Fig. 6C–G illustrated the particle internalization into the stimulated macrophages after seeding with 50 µg mL^{-1} of Ag_3PO_4/Pln nanocomposites for 3 days. The data presented in Fig. 6D depicts the macrophages treated with LPS/IFN-γ and subsequent seeding with the nanocomposites revealed that only Pln0 was able to penetrate into the cells (Fig. 6D).

NO is a powerful ROS generator in macrophages in the presence of stimulants, and thus the NO secretion from the

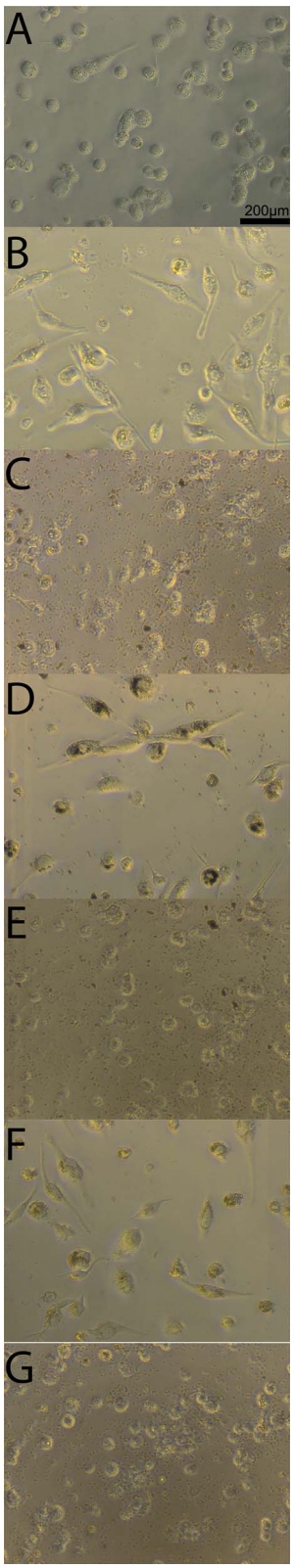

Fig. 6 Morphology of THP-1 derived macrophages after incubating with Pln or Ag_3PO_4 particles for 3 days. THP-1 cells have been induced by PMA, then stimulated by LPS (1 μg mL^{-1}) and IFN-γ (20 ng mL^{-1}). (A) THP-1 derived macrophage by PMA but without stimulation by LPS and IFN-γ. (B) THP-1 derived macrophage with LPS and IFN-γ stimulation; (C) THP-1 derived macrophage with LPS and IFN-γ stimulation and incubating with Ag_3PO_4; (D) THP-1 derived macrophage with LPS and IFN-γ stimulation and incubating with Pln0; (E) THP-1 derived macrophage with LPS and IFN-γ stimulation and incubating with Pln1; (F) THP-1 derived macrophage with LPS and IFN-γ stimulation and incubating with Pln2; (G) THP-1 derived macrophage with LPS and IFN-γ stimulation and incubating with Pln3. All the nanocomposites concentration in (C–G) groups were counted at a concentration of 50 particles per cell.

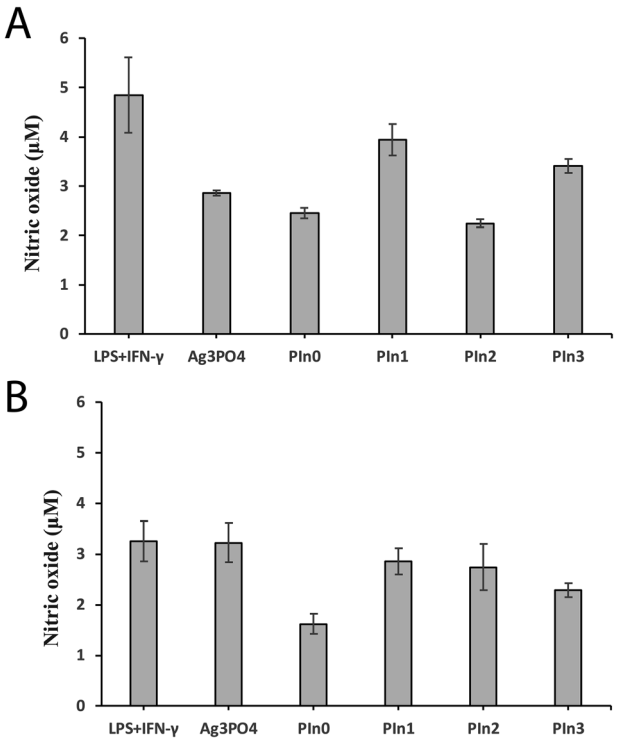

Fig. 7 NO secretion from THP-1 derived macrophage with LPS and IFN-γ stimulation and incubation with the various nanoparticles. (A) In the absence of light, (B) in the presence of light. All data are presented as mean ± SD ($n = 4$).

macrophages after seeding with the nanocomposites would help to predict the anti-inflammatory effect of the nanocomposites. Fig. 7A depicts the NO secretion from LPS treated macrophages along with the nanocomposites in absence of light. It is dramatically lowered after seeding with Pln2 (40%), Pln0 (50%). As compared to other components of the nanocomposites, bare Ag_3PO_4 did inhibit NO secretion by 60% efficacy. To validate this observation the same investigation was performed in the presence of light (Fig. 7B). In the latter case only Pln0 showed significant anti-inflammatory activity as compared to the other materials. This was due to rapid generation of ROS from these materials. DPPH is a stable free radical, which is used to assess the free radical scavenging capacity by the particles. As shown in Fig. 8, Ag_3PO_4 had the strongest free radical scavenging capacity, to 80% inhibition, whilst PIn1 can achieve nearly 70% inhibition. From conduction band edge potential of bare Ag_3PO_4 ($E_{CB} = 0.27$ eV) it was clear that bare Ag_3PO_4 cannot produce $O_2^{\bullet -}$ (E_H of $O_2^{\bullet -}/O_2 = -0.2$ eV) which promotes NO to yield different reactive nitrogen species. Thus, it can inhibit NO production in THP-I derived cells.

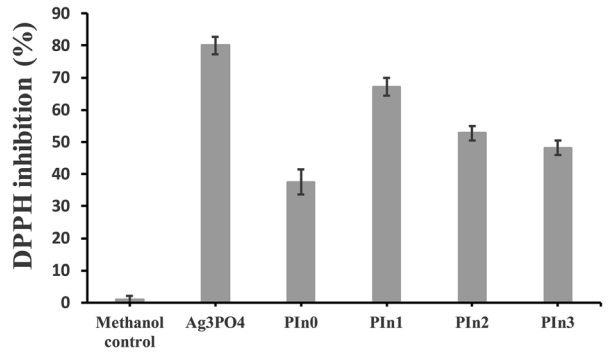

Fig. 8 Anti-oxidation measurement by DPPH radical scavenging capacity for the various particles. Data are presented as mean ± SD ($n = 4$).

Conclusions

The Ag_3PO_4/Pln nanocomposites presented here show long-term antibacterial activity in the dark. Specifically the composites with Pln content of 50% of Ag_3PO_4 show superior antibacterial activity with long-term durability. This particular composition also inhibited bacterial biofilms efficiently. Interestingly pure polyindole also exhibited antibacterial activity for a longer time period than that of pure Ag_3PO_4. The underlying factor for such long-term antibacterial activity is accounted for by intracellular ROS production from the composites. The composites with Pln content of 50% of Ag_3PO_4 generated the highest amount of intracellular ROS for a prolonged time period. Pure polyindole's antibacterial activity as well as the composite with the highest content of polyindole promoted membrane disintegration, which is the prime cause of their antibacterial activity. Additionally the composites exhibited anticancer activity with low toxicity towards other cells. THP-1 derived macrophages can be protected from LPS stimulation by composites with Pln contents of 25% of Ag_3PO_4 in the dark. The Ag_3PO_4/Pln nanocomposites are efficient antibacterial agents for long durations with a simultaneous anti-inflammatory response. In addition, the nanocomposites have potential for anticancer therapy. Clearly, the promise of these materials will need significantly more detailed studies, *e.g.* physicochemical (for example ESR),[80–83] *in vitro*,[84] *in silico*,[85–87] *in vivo* (in pre-clinical models, *e.g.* small mammals),[88] and thereafter clinical trials prior to translation to the clinic; such nanocomposites therefore have a variety of potential technical and medical applications.[89]

Conflicts of interest

There are no conflicts to declare.

Acknowledgements

We thank the Department of Science & Technology, Government of India, for financial support for S. P. through the DST-INSPIRE program (Grant No. DST/INSPIRE Fellowship/2014/82). We thank The Dowager Countess Eleanor Peel Trust for financial support to enable the purchase of a camera for the TEM. We acknowledge the support of a Lancaster University Faculty of Science and Technology Early Career Internal Grant and a Royal Society Research Grant (RG160449) to facilitate international collaborative research activities for J. G. H.

References

1 A. Bassegoda, K. Ivanova, E. Ramon and T. Tzanov, *Appl. Microbiol. Biotechnol.*, 2018, **102**, 2075.
2 I. A. Hassan, S. Sathasivam, S. P. Nair and C. J. Carmalt, *ACS Omega*, 2017, **2**, 4556.
3 S. J. Lam, N. M. O'Brien-Simpson, N. Pantarat, A. Sulistio, E. H. Wong, Y. Y. Chen, J. C. Lenzo, J. A. Holden, A. Blencowe, E. C. Reynolds and G. G. Qiao, *Nat. Microbiol.*, 2016, **1**, 16162.
4 D. Chen, Z. Wang, T. Ren, H. Ding, W. Yao, R. Zong and Y. Zhu, *J. Phys. Chem. C*, 2014, **118**, 15300.
5 H. Yin, P. S. Casey, M. J. McCall and M. Fenech, *Langmuir*, 2010, **26**, 15399.
6 S. Podder, D. Chanda, A. K. Mukhopadhyay, A. De, B. Das, A. Samanta, J. G. Hardy and C. K. Ghosh, *Inorg. Chem.*, 2018, **57**, 12727.
7 Y. H. Leung, A. M. Ng, X. Xu, Z. Shen, L. A. Gethings, M. T. Wong, C. M. Chan, M. Y. Guo, Y. H. Ng, A. B. Djurišić, P. K. Lee, W. K. Chan, L. H. Yu, D. L. Phillips, A. P. Ma and F. C. Leung, *Small*, 2014, **10**, 1171.
8 V. Lakshmi Prasanna and R. Vijayaraghavan, *Langmuir*, 2015, **31**, 9155.
9 W. Zhang, Y. Li, J. Niu and Y. Chen, *Langmuir*, 2013, **29**, 4647.
10 Y. Li, W. Zhang, J. Niu and Y. Chen, *ACS Nano*, 2012, **6**, 5164.
11 M. Fuji, M. Usui and S. Hayashi, *J. Appl. Phys.*, 2004, **95**, 3689.
12 J. Du and J. M. Gebicki, *Int. J. Biochem. Cell Biol.*, 2004, **36**, 2334.
13 Z. Tian, X. Li, Y. Ma, T. Chen, D. Xu, B. Wang, Y. Qu and Y. Gao, *ACS Appl. Mater. Interfaces*, 2017, **9**, 23342.
14 J. Gupta, P. Bhargava and D. Bahadur, *J. Mater. Chem. B*, 2015, **3**, 1968.
15 M. Arakha, M. Saleem, B. C. Mallick and S. Jha, *Sci. Rep.*, 2015, **5**, 9578.
16 S. Podder, S. Halder, A. Roychowdhury, D. Das and C. K. Ghosh, *J. Nanopart. Res.*, 2016, **18**, 294.
17 N. C. Raut, T. Matthews, P. K. Ajikumar, R. P. George, S. Dash and A. K. Tyagi, *RSC Adv.*, 2012, **2**, 10639.
18 M. Azimzadehirani, M. Elahifard, S. Haghighi and M. Gholami, *Photochem. Photobiol. Sci.*, 2013, **12**, 1787.
19 S. H. Hwang, J. Song, Y. Jung, O. Y. Kweon, H. Song and J. Jang, *Chem. Commun.*, 2011, **47**, 9164.
20 G. Tong, F. Du, W. Wu, R. Wu, F. Liu and Y. Liang, *J. Mater. Chem. B*, 2013, **1**, 2647.
21 O. Akhavan, R. Azimirad, S. Safa and E. Hasani, *J. Mater. Chem.*, 2011, **21**, 9634.
22 C. Piccirillo, R. A. Pinto, D. M. Tobaldi, R. C. Pullar, J. A. Labrincha, M. M. E. Pintado and P. M. L. Castro, *J. Photochem. Photobiol., A*, 2014, **296**, 40.

23 A. Herman and A. P. Herman, *J. Nanosci. Nanotechnol.*, 2014, **14**, 946.
24 S. M. Dizaj, F. Lotfipour, M. Barzegar-Jalali, M. H. Zarrintan and K. Adibkia, *Mater. Sci. Eng., C*, 2014, **44**, 278.
25 M. Bhamidipati and L. Fabris, *Bioconjugate Chem.*, 2017, **28**, 449.
26 M. Li, L. Zhu and D. Lin, *Environ. Sci. Technol.*, 2011, **45**, 1977.
27 M. Lu, Y. Wang, M. Jiang and X. Yao, *ACS Appl. Mater. Interfaces*, 2016, **8**, 23580.
28 X. Wang, F. Yang, W. Yang and X. Yang, *Chem. Commun.*, 2007, 4419.
29 W. Shi, C. Li, M. Li, X. Zong, D. Han and Y. Chen, *Appl. Microbiol. Biotechnol.*, 2016, **100**, 5059.
30 M. Lv, Y. He, Q. Huang, W. Hu, D. Li, C. Fan and S.-T. Lee, *Adv. Mater.*, 2010, **22**, 5463.
31 R. Zao, W. Kong, M. Sun, Y. Yang, W. Liu, M. Lv, S. Song, L. Wang, H. Song and R. Hao, *ACS Appl. Mater. Interfaces*, 2018, **10**, 17617.
32 T. Feng, J. Liang, Z. Ma, M. Li and M. Tong, *Colloids Surf., B*, 2018, **167**, 275.
33 E. L. Cyphert and H. A. von Recum, *Exp. Biol. Med.*, 2017, **242**, 788.
34 P. Sautrot-Ba, N. Razza, L. Breloy, S. Abbad Andaloussi, A. Chiappone, M. Sangermano, C. Hélary, S. Belbekhouche, T. Coradin and D.-L. Versace, *J. Mater. Chem. B*, 2019, **7**, 6526.
35 T. Li, F. Li, W. Xiang, Y. Yi, Y. Chen, L. Cheng, Z. Liu and H. Xu, *ACS Appl. Mater. Interfaces*, 2016, **8**, 22106.
36 L. Xiao, L. Gu, S. P. Howell and M. J. Sailor, *ACS Nano*, 2011, **5**, 3651.
37 F. Li, T. Li, X. Han, H. Zhuang, G. Nie and H. Xu, *ACS Biomater. Sci. Eng.*, 2018, **4**, 1954.
38 H. Agarwal, A. Nakara and V. K. Shanmugam, *Biomed. Pharmacother.*, 2019, **109**, 2561.
39 C. F. Borgognoni, J. H. Kim, V. Zucolotto, H. Fuchs and K. Riehemann, *Artif. Cells, Nanomed., Biotechnol.*, 2018, **46**, S694.
40 G. Giacalone, N. Tsapis, L. Mousnier, H. Chacun and E. Fattal, *Materials*, 2018, **11**, 1845.
41 W. Zhang, S. Hu, J.-J. Yin, W. He, W. Lu, M. Ma, N. Gu and Y. Zhang, *J. Am. Chem. Soc.*, 2016, **138**, 5860.
42 M. Sriramulu and S. Sumathi, *Adv. Nat. Sci.: Nanosci. Nanotechnol.*, 2017, **8**, 045012.
43 M. Ramar, B. Manikandan, T. Raman, K. Arunagirinathan, N. M. Prabhu, M. J. Basu, M. Perumal, S. Palanisamy and A. Munusamy, *Spectrochim. Acta, Part A*, 2015, **138**, 120.
44 M. Govindappa, B. Hemashekhar, M.-K. Arthikala, V. Ravishankar Rai and Y. L. Ramachandra, *Results Phys.*, 2018, **9**, 400.
45 El-R. Kenawy, S. D. Worley and R. Broughton, *Biomacromolecules*, 2007, **8**, 1359–1384.
46 X. Liang, M. Sun, L. Li, R. Qiao, K. Chen, Q. Xiao and F. Xu, *Dalton Trans.*, 2012, **41**, 2804.
47 W. Xiao, J. Xu, X. Liu, Q. Hu and J. Huang, *J. Mater. Chem. B*, 2013, **1**, 3477.
48 M. Shoeb, M. Mobin, M. A. Rauf, M. Owais and A. H. Naqvi, *ACS Omega*, 2018, **3**, 9431.
49 R. Hassanien, M. Al-Hinai, S. A. F. Al-Said, R. Little, L. Šiller, N. G. Wright, A. Houlton and B. R. Horrocks, *ACS Nano*, 2010, **4**, 2149.
50 A. Kumar, L. Joshi and R. Prakash, *Ind. Eng. Chem. Res.*, 2013, **52**, 9374.
51 L. Liu, J. Liu and D. S. Sun, *Catal. Sci. Technol.*, 2012, **2**, 2525.
52 B. Panigrahy and S. Srivastava, *New J. Chem.*, 2016, **40**, 3370.
53 R. Guo, J. Wu, A. Xu, X. Huang, H. Zhu, R. Jiang, Y. Lin and F. Guo, *RSC Adv.*, 2016, **6**, 114818.
54 X. Chen, Y. Dai and X. Wang, *J. Alloys Compd.*, 2015, **649**, 910.
55 Q. Zhou, D. Zhu, X. Ma, J. Xu, W. Zhou and F. Zhao, *RSC Adv.*, 2016, **6**, 29840.
56 Y. Bu and Z. Chen, *ACS Appl. Mater. Interfaces*, 2014, **6**, 17589–17598.
57 Clinical and Laboratory Standards Institute. *M2-A9. Performance standards for antimicrobial disk susceptibility tests; approved standard*, Clinical and Laboratory Standards Institute, Wayne, PA, 9th edn. 2006.
58 R. Roy, M. Tiwari, G. Donelli and V. Tiwari, *Virulence*, 2018, **9**, 522.
59 E. Burton, N. Yakandawala, K. LoVetri and M. S. Madhyastha, *J. Ind. Microbiol. Biotechnol.*, 2007, **34**, 1.
60 M. S. Islas, J. J. Martínez Medina, L. L. López Tévez, T. Rojo, L. Lezama, M. Griera Merino, L. Calleros, M. A. Cortes, M. Rodriguez Puyol, G. A. Echeverría, O. E. Piro, E. G. Ferrer and P. A. M. Williams, *Inorg. Chem.*, 2014, **53**, 5724.
61 L. Zimmermann, I. Das, J. Désiré, G. Sautrey, V. R. S. Barros, M. El Khoury, M.-P. Mingeot-Leclerc and J.-L. Décout, *J. Med. Chem.*, 2016, **59**, 9350.
62 J. C. Stockert, R. W. Horobin, L. L. Colombo and A. Blázquez-Castro, *Acta Histochem.*, 2018, **120**, 159.
63 G. Botelho, J. Andres, L. Gracia, L. S. Matos and E. Longo, *ChemPlusChemc*, 2016, **81**, 202.
64 J. Bhadra, N. J. Al-Thani, S. Karmakar and N. K. Madia, *Arabian J. Chem.*, 2019, **12**, 4848.
65 J. J. Liu, X. L. Fu, S. F. Chen and Y. F. Zhu, *Appl. Phys. Lett.*, 2011, **99**, 191903.
66 Z. Mei, S. Ouyang, D.-M. Tang, T. Kako, D. Golberg and J. a. Ye, *Dalton Trans.*, 2013, **42**, 2687.
67 H. Cheng, B. Huang, X. Qin, X. Zhang and Y. Dai, *Chem. Commun.*, 2012, **48**, 97.
68 R. Y. Pelgrift and A. J. Friedman, *Adv. Drug Delivery Rev.*, 2013, **65**, 1803.
69 A. Samanta, S. Podder, C. K. Ghosh, M. Bhattacharya, J. Ghosh, A. K. Mallik, A. Dey and A. K. Mukhopadhyay, *J. Mech. Behav. Biomed. Mater.*, 2017, **72**, 110.
70 K. R. Raghupathi, R. T. Koodali and A. C. Manna, *Langmuir*, 2011, **27**, 4020.
71 E. Kłodzińska, M. Szumski, E. Dziubakiewicz, K. Hrynkiewicz, E. Skwarek, W. Janusz and B. Buszewski, *Electrophoresis*, 2010, **31**, 1590.
72 N. Stobie, B. Duffy, D. E. McCormack, J. Colreavy, M. Hidalgo, P. McHale and S. J. Hinder, *Biomaterials*, 2008, **29**, 963.

73 S. Jaiswal, K. Bhattacharya, P. McHale and B. Duffy, *J. Mater. Sci.: Mater. Med.*, 2015, **26**, 52.
74 S. Megarajan, M. Vidhyalakshmi, K. B. A. Ahmed, V. Murali, B. R. S. Niranjani, N. Saisubramanian and V. Anbazhagan, *RSC Adv.*, 2016, **6**, 87513.
75 K. Vijayalakshmi and D. Sivaraj, *RSC Adv.*, 2016, **6**, 9663.
76 R. Zhao, M. Lv, Y. Li, M. Sun, W. Kong, L. Wang, S. Song, C. Fan, L. Jia, S. Qiu, Y. Sun, H. Song and R. Hao, *ACS Appl. Mater. Interfaces*, 2017, **9**, 15328.
77 Y. Chong, C. Ge, G. Fang, X. Tian, X. Ma, T. Wen, W. G. Wamer, C. Chen, Z. Chai and J.-J. Yin, *ACS Nano*, 2016, **10**, 8690.
78 C. Atanu and N. R. Jana, *ACS Appl. Mater. Interfaces*, 2017, **9**, 41807.
79 B. Wang, W. Lin, Z. Mao and C. Gao, *J. Mater. Chem. B*, 2018, **6**, 3145.
80 N. K. Eswar, V. V. Katkar, P. C. Ramamurthy and G. Madras, *Ind. Eng. Chem. Res.*, 2015, **54**, 8031.
81 X. Yu, Y. Lin, H. Liu, C. Yang, Y. Peng, C. Du, S. Wu, X. Li and Y. Zhong, *J. Colloid Interface Sci.*, 2020, **561**, 379–395.
82 J. Jin, M. Liu, L. Feng, H. Wang, Y. Wang, T. A. H. Nguyen, Y. Wang, J. Lu, Y. Li and M. Bao, *Sci. Total Environ.*, 2019, **695**, 133694.
83 Z. Duan, L. Deng, Z. Shi, H. Zhang, H. Zeng and J. Crittenden, *J. Colloid Interface Sci.*, 2019, **534**, 270.
84 K. P. Steckiewicz, J. Zwara, M. Jaskiewicz, S. Kowalski, W. Kamysz, A. Zaleska-Medynska and I. Inkielewicz-Stepniak, *Oxid. Med. Cell. Longevity*, 2019, 6740325.
85 H. Katsumata, T. Sakai, T. Suzuki and S. Kaneco, *Ind. Eng. Chem. Res.*, 2014, **53**, 8018.
86 R. A. Roca, J. C. Sczancoski, I. C. Nogueira, M. T. Fabbro, H. C. Alves, L. Gracia, L. P. S. Santos, C. P. de Sousa, J. Andrés, G. E. Luz Jr, E. Longo and L. S. Cavalcante, *Catal. Sci. Technol.*, 2015, **5**, 4091.
87 A. B. Trench, T. R. Machado, A. F. Gouveia, M. Assis, L. Guerreiroda Trindade, C. Santos, A. Perrin, C. Perrin, M. Oliva, J. Andrés and E. Longo, *Appl. Catal., B*, 2018, **238**, 198.
88 C. Zhang, J. Wang, R. Chi, J. Shi, Y. Yang and X. Zhang, *Mater. Des.*, 2019, **183**, 108166.
89 Rita, S. Mehtab, M. G. H. Zaidi, K. Singhal, B. Arya and T. I. Siddiqui, *Mater. Sci. Res. India*, 2019, **16**, 97.